SUPPORTING INFORMATION

New opportunities for tailored nanoparticle catalysts through exsolution from inherently disordered defect fluorite-type oxides

William S. J. Skinner,*[a] Eleonora Calì,[b] Angelos K. Bonis,[c] Gwilherm Kerherve,[a] Kalliopi Kousi[c] and David J. Payne*[a,d]

[a]Department of Materials, Imperial College London, Exhibition Road, London SW7 2AZ, United Kingdom. E-mail: d.payne@imperial.ac.uk.

[b]Department of Applied Science and Technology, Politecnico di Torino, Corso Duca degli Abruzzi, 24, Turin 10129, Italy.

[c]University of Surrey, School of Chemistry and Chemical Engineering, University of Surrey, Guildford, GU2 7XH, United Kingdom

[d]NEOM Education, Research, and Innovation Foundation, Al Khuraybah, Tabuk 49643-9136, Saudi Arabia

*Corresponding authors: William S. J. Skinner and David J. Payne

E-mails: William.skinner17@imperial.ac.uk; d.payne@imperial.ac.uk.

Experimental

X-ray diffraction

Data processing

Powder X-ray diffraction data was processed by setting the base line to zero and normalising to the highest intensity peak (the reflection indexed to the (111) plane of $Y_2Zr_{2-x}Ru_xO_7$). The scale of all powder X-ray diffraction plots is linear.

Indexed Peaks

Table S1. Indexed X-ray diffraction peaks for $Y_2Zr_2O_7$, alongside their interplanar spacings and the calculated interplanar spacings based on the fitted unit cell (space group *Fm*-3*m*, a = 5.201 ± 0.002 Å).

Peak	$2\theta_{obs}$ (°)	h	k	l	D_{obs} (Å)	D_{calc} (Å)	D_{obs} - D_{calc} (Å)
1	29.8 ± 0.1	1	1	1	3.001 ± 0.020	3.003	-0.002
2	34.5 ± 0.1	2	0	0	2.601 ± 0.015	2.601	0.000
3	49.6 ± 0.1	2	2	0	1.838 ± 0.007	1.839	-0.001
4	58.9 ± 0.1	3	1	1	1.568 ± 0.005	1.568	0.000
5	61.8 ± 0.1	2	2	2	1.501 ± 0.004	1.501	-0.001
6	72.7 ± 0.1	4	0	0	1.300 ± 0.003	1.300	0.000
7	80.5 ± 0.1	3	3	1	1.193 ± 0.002	1.193	0.000
8	83.0 ± 0.1	4	2	0	1.163 ± 0.002	1.163	0.000
9	93.1 ± 0.1	4	2	2	1.062 ± 0.002	1.062	0.000
10	100.7 ± 0.1	3	3	3	1.001 ± 0.001	1.001	0.000

Table S2. Indexed X-ray diffraction peaks for $Y_2Zr_{1.9}Ru_{0.1}O_7$, alongside their interplanar spacings and the calculated interplanar spacings based on the fitted unit cell (space group *Fm*-3*m*, a = 5.200 ± 0.002 Å).

Peak	2θ (°)	h	k	l	D_{obs} (Å)	D_{calc} (Å)	$\lvert D_{obs} - D_{calc} \rvert$ (Å)
1	29.8 ± 0.1	1	1	1	3.003 ± 0.020	3.002	0.001
2	34.5 ± 0.1	2	0	0	2.601 ± 0.015	2.600	0.001
3	49.6 ± 0.1	2	2	0	1.838 ± 0.007	1.839	0.000

4	58.9 ± 0.1	3	1	1	1.568 ± 0.005	1.568	0.000
5	61.8 ± 0.1	2	2	2	1.501 ± 0.004	1.501	0.000
6	72.7 ± 0.1	4	0	0	1.300 ± 0.003	1.300	0.000
7	80.5 ± 0.1	3	3	1	1.193 ± 0.002	1.193	0.000
8	83.1 ± 0.1	4	2	0	1.163 ± 0.002	1.163	0.000
9	93.1 ± 0.1	4	2	2	1.062 ± 0.002	1.061	0.000
10	100.8 ± 0.1	3	3	3	1.001 ± 0.001	1.001	0.000

Table S3. Indexed X-ray diffraction peaks for $Y_2Zr_{1.8}Ru_{0.2}O_7$, alongside their interplanar spacings and the calculated interplanar spacings based on the fitted unit cell (space group *Fm*-3*m*, a = 5.196 ± 0.002 Å).

Peak	2θ (°)	h	k	l	D_{obs} (Å)	D_{calc} (Å)	$\lvert D_{obs} - D_{calc} \rvert$ (Å)
1	29.8 ± 0.1	1	1	1	2.998 ± 0.020	3.000	-0.002
2	34.5 ± 0.1	2	0	0	2.600 ± 0.015	2.598	0.002
3	49.6 ± 0.1	2	2	0	1.838 ± 0.007	1.837	0.001
4	59.0 ± 0.1	3	1	1	1.566 ± 0.005	1.567	-0.001
5	61.8 ± 0.1	2	2	2	1.501 ± 0.004	1.500	0.001
6	72.8 ± 0.1	4	0	0	1.299 ± 0.003	1.299	0.000
7	80.6 ± 0.1	3	3	1	1.192 ± 0.002	1.192	0.000
8	83.1 ± 0.1	4	2	0	1.162 ± 0.002	1.162	0.000
9	93.3 ± 0.1	4	2	2	1.060 ± 0.002	1.061	0.000
10	100.9 ± 0.1	3	3	3	1.000 ± 0.001	1.000	0.000

Table S4. Indexed X-ray diffraction peaks for $Y_2Zr_2O_7$-R10, alongside their interplanar spacings and the calculated interplanar spacings based on the fitted unit cell (space group *Fm*-3*m*, a = 5.202 ± 0.002 Å).

Peak	$2\theta_{obs}$ (°)	h	k	l	D_{obs} (Å)	D_{calc} (Å)	$D_{obs} - D_{calc}$ (Å)
1	29.7 ± 0.1	1	1	1	3.008 ± 0.020	3.003	0.005
2	34.5 ± 0.1	2	0	0	2.600 ± 0.015	2.601	-0.001
3	49.6 ± 0.1	2	2	0	1.838 ± 0.007	1.839	-0.001
4	58.9 ± 0.1	3	1	1	1.568 ± 0.005	1.568	0.000
5	61.8 ± 0.1	2	2	2	1.501 ± 0.004	1.502	-0.001
6	72.7 ± 0.1	4	0	0	1.301 ± 0.003	1.300	0.000
7	80.5 ± 0.1	3	3	1	1.193 ± 0.002	1.193	0.000
8	83.0 ± 0.1	4	2	0	1.163 ± 0.002	1.163	0.000
9	93.1 ± 0.1	4	2	2	1.062 ± 0.002	1.062	0.000
10	100.7 ± 0.1	3	3	3	1.001 ± 0.001	1.001	0.000

Table S5. Indexed X-ray diffraction peaks for $Y_2Zr_{1.9}Ru_{0.1}O_7$-R10, alongside their interplanar spacings and the calculated interplanar spacings based on the fitted unit cell (space group *Fm*-3*m*, a = 5.207 ± 0.002 Å).

Peak	2θ (°)	h	k	l	D_{obs} (Å)	D_{calc} (Å)	$\lvert D_{obs} - D_{calc} \rvert$ (Å)
1	29.7 ± 0.1	1	1	1	3.008 ± 0.020	3.006	0.002
2	34.4 ± 0.1	2	0	0	2.607 ± 0.015	2.604	0.003

3	49.5 ± 0.1	2	2	0	1.841 ± 0.007	1.841	0.000
4	58.8 ± 0.1	3	1	1	1.570 ± 0.005	1.570	0.000
5	61.7 ± 0.1	2	2	2	1.503 ± 0.004	1.503	0.000
6	72.6 ± 0.1	4	0	0	1.302 ± 0.003	1.302	0.000
7	80.4 ± 0.1	3	3	1	1.194 ± 0.002	1.195	0.000
8	82.9 ± 0.1	4	2	0	1.165 ± 0.002	1.164	0.000
9	93.0 ± 0.1	4	2	2	1.063 ± 0.002	1.063	0.000
10	100.6 ± 0.1	3	3	3	1.002 ± 0.001	1.002	0.000

Table S6. Indexed X-ray diffraction peaks for $Y_2Zr_{1.8}Ru_{0.2}O_7$-R04, alongside their interplanar spacings and the calculated interplanar spacings based on the fitted unit cell (space group *Fm*-3*m*, a = 5.195 ± 0.002 Å).

Peak	2θ (°)	h	k	l	D_{obs} (Å)	D_{calc} (Å)	$\lvert D_{obs} - D_{calc} \rvert$ (Å)
1	29.8 ± 0.1	1	1	1	2.998 ± 0.020	2.999	-0.001
2	34.5 ± 0.1	2	0	0	2.600 ± 0.015	2.598	0.002
3	49.6 ± 0.1	2	2	0	1.838 ± 0.007	1.837	0.001
4	59.0 ± 0.1	3	1	1	1.566 ± 0.005	1.566	-0.001
5	61.9 ± 0.1	2	2	2	1.499 ± 0.004	1.500	-0.001
6	72.8 ± 0.1	4	0	0	1.299 ± 0.003	1.299	0.000
7	80.6 ± 0.1	3	3	1	1.192 ± 0.002	1.192	0.000
8	83.1 ± 0.1	4	2	0	1.162 ± 0.002	1.162	0.001
9	93.3 ± 0.1	4	2	2	1.060 ± 0.002	1.060	0.000
10	100.9 ± 0.1	3	3	3	1.000 ± 0.001	1.000	0.000

Table S7. Indexed X-ray diffraction peaks for $Y_2Zr_{1.8}Ru_{0.2}O_7$-R06, alongside their interplanar spacings and the calculated interplanar spacings based on the fitted unit cell (space group *Fm*-3*m*, a = 5.194 ± 0.002 Å).

Peak	2θ (°)	h	k	l	D_{obs} (Å)	D_{calc} (Å)	$\lvert D_{obs} - D_{calc} \rvert$ (Å)
1	29.8 ± 0.1	1	1	1	2.998 ± 0.020	2.999	-0.001
2	34.5 ± 0.1	2	0	0	2.600 ± 0.015	2.598	0.002
3	49.6 ± 0.1	2	2	0	1.838 ± 0.007	1.837	0.001
4	59.0 ± 0.1	3	1	1	1.566 ± 0.005	1.566	-0.001
5	61.9 ± 0.1	2	2	2	1.499 ± 0.004	1.500	-0.001
6	72.8 ± 0.1	4	0	0	1.299 ± 0.003	1.299	0.000
7	80.6 ± 0.1	3	3	1	1.192 ± 0.002	1.192	0.000
8	83.1 ± 0.1	4	2	0	1.162 ± 0.002	1.162	0.001
9	93.3 ± 0.1	4	2	2	1.060 ± 0.002	1.060	0.000
10	100.9 ± 0.1	3	3	3	1.000 ± 0.001	1.000	0.000

Table S8. Indexed X-ray diffraction peaks for $Y_2Zr_{1.8}Ru_{0.2}O_7$-R08, alongside their interplanar spacings and the calculated interplanar spacings based on the fitted unit cell (space group *Fm*-3*m*, a = 5.202 ± 0.002 Å).

Peak	2θ (°)	h	k	l	D_{obs} (Å)	D_{calc} (Å)	$\lvert D_{obs} - D_{calc} \rvert$ (Å)
1	29.7 ± 0.1	1	1	1	3.008 ± 0.020	3.003	0.005

2	34.5 ± 0.1	2	0	0	2.600 ± 0.015	2.601	-0.001
3	49.6 ± 0.1	2	2	0	1.838 ± 0.007	1.839	-0.001
4	58.9 ± 0.1	3	1	1	1.568 ± 0.005	1.568	0.000
5	61.8 ± 0.1	2	2	2	1.501 ± 0.004	1.502	-0.001
6	72.7 ± 0.1	4	0	0	1.301 ± 0.003	1.300	0.000
7	80.5 ± 0.1	3	3	1	1.193 ± 0.002	1.193	0.000
8	83.0 ± 0.1	4	2	0	1.163 ± 0.002	1.163	0.000
9	93.1 ± 0.1	4	2	2	1.062 ± 0.002	1.062	0.000
10	100.7 ± 0.1	3	3	3	1.001 ± 0.001	1.001	0.000

Table S9. Indexed X-ray diffraction peaks for $Y_2Zr_{1.8}Ru_{0.2}O_7$-R10, alongside their interplanar spacings and the calculated interplanar spacings based on the fitted unit cell (space group *Fm*-3*m*, a = 5.211 ± 0.002 Å).

Peak	2θ (°)	h	k	l	D_{obs} (Å)	D_{calc} (Å)	$\lvert D_{obs} - D_{calc} \rvert$ (Å)
1	29.7 ± 0.1	1	1	1	3.008 ± 0.020	3.009	-0.001
2	34.4 ± 0.1	2	0	0	2.607 ± 0.015	2.606	0.001
3	49.5 ± 0.1	2	2	0	1.841 ± 0.007	1.842	-0.001
4	58.8 ± 0.1	3	1	1	1.570 ± 0.005	1.571	-0.001
5	61.7 ± 0.1	2	2	2	1.503 ± 0.004	1.504	-0.001
6	72.5 ± 0.1	4	0	0	1.304 ± 0.003	1.303	0.001
7	80.3 ± 0.1	3	3	1	1.196 ± 0.002	1.195	0.000
8	82.8 ± 0.1	4	2	0	1.166 ± 0.002	1.165	0.001
9	92.9 ± 0.1	4	2	2	1.064 ± 0.002	1.064	0.000
10	100.5 ± 0.1	3	3	3	1.003 ± 0.001	1.003	0.000

Fitted Unit Cells

Table S10. Unit cells fitted with the UnitCell software using the indexed peaks in Tables S1-9, with calculated lattice parameters alongside corresponding standard deviations and 95% confidence intervals. To account for the broad peak widths and the challenge in accurately identifying peak positions, the representative uncertainty in the peak position was set to a relatively conservative value of 0.1° 2θ.

Sample	Space Group	a (Å)	σ_a (Å)	95% CI (Å)
$Y_2Zr_2O_7$	*Fm*-3*m*	5.201	0.002	0.004
$Y_2Zr_{1.9}Ru_{0.1}O_7$	*Fm*-3*m*	5.200	0.002	0.004
$Y_2Zr_{1.8}Ru_{0.2}O_7$	*Fm*-3*m*	5.196	0.002	0.004
$Y_2Zr_2O_7$-R10	*Fm*-3*m*	5.202	0.002	0.004
$Y_2Zr_{1.9}Ru_{0.1}O_7$-R10	*Fm*-3*m*	5.207	0.002	0.004
$Y_2Zr_{1.8}Ru_{0.2}O_7$-R04	*Fm*-3*m*	5.195	0.002	0.004
$Y_2Zr_{1.8}Ru_{0.2}O_7$-R06	*Fm*-3*m*	5.194	0.002	0.004
$Y_2Zr_{1.8}Ru_{0.2}O_7$-R08	*Fm*-3*m*	5.202	0.002	0.004
$Y_2Zr_{1.8}Ru_{0.2}O_7$-R10	*Fm*-3*m*	5.211	0.002	0.004

X-ray photoelectron spectroscopy

Peak fitting models

Table S11. Peak fitting model (XPS, Thermo Avantage) for the overlapping Ru 3*d* and C 1*s* core levels, with a Shirley background applied.

Ref.	Peak Label	Position (eV)	FWHM (eV)	Area Ratio	L/G Mix (%) (Convolve)	Tail Mix (%)	Tail Height (%)	Tail Exp.
A	Ru3d5 Ru 0	280.0 (± 0.2)	0.9 : 1.2	-	20	78	0	0.054
B	Ru3d3 Ru 0	A + 4.14	A * 1.78	A * 0.667	20	54	0	0.07
C	Ru3d5 Ru 3	A + 0.90 (± 0.2)	1.1 : 1.4	-	20	0	0	0
D	Ru3d3 Ru 3	C + 4.10	C * 1	C * 0.667	20	0	0	0
E	Ru3d5 Ru 4	C + 1.35 (± 0.1)	C * 1	-	20	0	0	0
F	Ru3d3 Ru 4	E + 4.13	C * 1	D * 0.667	20	0	0	0
G	Ru3d5 Ru 5	C + 2.55 (± 0.1)	C * 1	-	20	0	0	0
H	Ru3d3 Ru 5	G + 4.18	C * 1	G * 0.667	20	0	0	0
I	C1s C-C	284.4 : 284.8	1.3 : 1.6	-	20	0	0	0
J	C1s C-O	I + 1.40 (± 0.1)	I * 1	-	20	0	0	0
K	C1s C=O	I + 3.0 (± 0.1)	I * 1	-	20	0	0	0
L	C1s O-C=O	A + 9.30 (± 0.2)	I * 1 (± 0.2)	-	20	0	0	0

Table S12. Peak fitting model (XPS, Thermo Avantage) for the O 1*s* core level, with a Shirley background applied.

Ref.	Peak Label	Position (eV)	FWHM (eV)	Area Ratio	L/G Mix (%) (Convolve)	Tail Mix (%)	Tail Height (%)	Tail Exp.
A	O1s M-O	-	0.9 : 1.4	-	20	0	0	0
B	O1s O-H	A + 1.40	A * 1	-	20	0	0	0
C	O1s C-O	A + 2.0	A * 1	-	20	0	0	0
D	O1s O-C=O	C + 2.55	A * 1	-	20	0	0	0
E	O1s SiO2	C + 3.60	A * 1	-	20	0	0	0

Table S13. Peak fitting model (XPS, Thermo Avantage) for the Y 3*d* and Zr 3*d* core levels, with a Shirley background applied.

Ref.	Peak Label	Position (eV)	FWHM (eV)	Area Ratio	L/G Mix (%) (Convolve)	Tail Mix (%)	Tail Height (%)	Tail Exp.
A	Y3d5 Y-O	-	0.9 : 1.4	-	20	0	0	0
B	Y3d3 Y-O	A + 2.06	A * 1	A * 0.667	20	0	0	0
C	Y3d5 YCO3	A + 1.25	A * 1	-	20	0	0	0
D	Y3d3 YCO3	C + 1.95	A * 1	C * 0.667	20	0	0	0
E	Zr3d5 Zr-O	-	0.5 : 1.5	-	20	0	0	0
F	Zr3d3 Zr-O	E + 2.38	E * 1	E * 0.667	20	0	0	0

Data processing

XPS data was processed by (1) setting the base line to zero, (2) normalising the intensity to that of the Y $3d_{5/2}$ signal assigned to lattice Y^{3+}, and (3) calibrating the binding energy to that of the Zr $3d_{5/2}$ signal of lattice Zr^{4+}, which is set to 181.8 eV for $Y_2Zr_2O_7$ and 181.4 eV for $Y_2Zr_{2-x}Ru_xO_7$. The Y $3d_{5/2}$ signal assigned to lattice Y^{3+} was chosen for intensity normalisation because it is expected to remain fairly stable between samples of different composition and treatment history. The Zr $3d_{5/2}$ signal assigned to lattice Zr^{4+} was chosen for binding energy calibration to address the uncertainty in reliability of using the C 1*s* C-C peak in comparing samples where reduction may induce changes in the Fermi level, and thus the assumption of a common Fermi level between adventitious carbon and sample may no longer apply, as well as the challenge in accurately fitting the C 1*s* C-C peak as a result of direct overlap with the Ru 3*d* core level region. We approached this by determining the binding energy position of the Zr $3d_{5/2}$ Zr^{4+} signal for each of the $Y_2Zr_{2-x}Ru_xO_7$ samples before any reducing treatment, which we believe can be reliably calibrated to the binding energy of the C 1*s* C-C peak. The position of the Zr $3d_{5/2}$ Zr^{4+} signal was positioned at 181.8 eV for $Y_2Zr_2O_7$ and 181.4 eV for $Y_2Zr_{1.9}Ru_{0.1}O_7$ and $Y_2Zr_{1.8}Ru_{0.2}O_7$, with the shift in binding energy of 0.4 eV expected to relate to the partial substitution of Zr cations by Ru cations in the lattice. These values are both well within the range of Zr $3d_{5/2}$ binding energies observed previously for Zr^{4+}.[1,2] A key assumption underpinning the use of these peak positions as our binding energy reference is that they will not vary considerably following reductive treatment. This assumption was found to hold well in the case of $Y_2Zr_2O_7$, where the position of the Zr $3d_{5/2}$ signal of lattice Zr^{4+} was stable at approximately 181.8 eV before and after reduction at 1000 °C, representing the most extreme reducing conditions employed in this study; we anticipate that it also holds well in the case of both $Y_2Zr_{1.9}Ru_{0.1}O_7$ and $Y_2Zr_{1.8}Ru_{0.2}O_7$. Our results appear to support the reliability of this approach to binding energy calibration, as the binding energy position of the peak attributed to exsolved Ru metal is stable at its expected position of 280 ± 0.1 eV.[3]

Quantification

Table S14. Quantification data for $Y_2Zr_{1.9}Ru_{0.1}O_7$ before and after reduction at temperatures in the range 400 – 1000 °C. Relative atomic percentage calculations were performed using the TPP-2M-corrected areas of the relevant peaks and their respective sensitivity factors as provided by the Thermo Avantage software (5.348 for Zr $3d_{5/2}$, 8.744 for Ru$3d_{5/2}$).

Reduction Temperature (°C)	Relative Atomic Percentage				
	Zr^{4+}	$Ru^{4+/5}$	Ru^{3+}	Ru^0	Total Ru
0	94.97	3.48	1.55	0.00	5.03
400	94.90	2.34	2.12	0.64	5.10
500	94.97	1.88	2.03	1.13	5.04
600	95.15	1.67	1.81	1.38	4.86
700	95.15	1.94	1.27	1.64	4.85
800	95.08	1.08	1.70	2.15	4.93
900	95.14	0.60	0.75	3.51	4.86
1000	94.17	0.35	1.12	4.35	5.82

Table S15. Quantification data for $Y_2Zr_{1.8}Ru_{0.2}O_7$ before and after reduction at temperatures in the range 400 – 1000 °C. Relative atomic percentage calculations were performed using the TPP-2M-corrected areas of the relevant peaks and their respective sensitivity factors as provided by the Thermo Avantage software (5.348 for Zr 3$d_{5/2}$, 8.744 for Ru3$d_{5/2}$).

Reduction Temperature (°C)	Relative Atomic Percentage				
	Zr^{4+}	$Ru^{4+/5}$	Ru^{3+}	Ru^{0}	Total Ru
0	91.05	5.78	3.17	0.00	8.95
400	90.62	3.81	3.81	1.76	9.38
500	90.33	3.41	3.13	3.13	9.67
600	90.67	4.99	2.31	2.03	9.33
700	90.50	1.90	3.17	4.43	9.50
800	90.39	1.18	2.09	6.35	9.62
900	89.68	0.63	2.33	7.36	10.32
1000	90.34	0.43	1.35	7.83	9.61

Near-ambient pressure X-ray photoelectron spectroscopy

Measurement protocol

The NAP-XPS measurement protocol used to probe exsolution *in situ* is as follows. The sample was first held and measured under oxidising conditions (0.5 mbar O_2, 400 °C) to fully oxidise the sample and remove any adventitious carbon that may interfere with interpretation of the Ru 3*d* core level region, without any risk of sample reduction. The temperature was then ramped down, held and measured under "inert" conditions (0.5 mbar Ar, 100 °C). The temperature was then increased rapidly (25 °C/min) under 0.5 mbar Ar to 300 °C before switching the atmosphere to 0.5 mbar H_2 and immediately beginning to measure. Upon completion of measurements under H_2 at 300 °C, the temperature was increased rapidly (25 °C/min) to 400 °C and measurements were started immediately. This was carried out again for measurements at 500 °C. To enable comparison between measurements, the different spectra were calibrated by setting the binding energy position of Zr 3$d_{5/2}$ to 181.4 eV (the position observed in *ex situ* measurements).

Peak fitting model

Table S16. Peak Fitting Model (NAP-XPS, CasaXPS) applied for the overlapping Ru 3*d* and C 1*s* core levels, with a Shirley background applied.

Ref.	Peak Label	Position (eV)	FWHM (eV)	Area Ratio	Line Shape
A	Ru3d5 Ru 0	-	0.9 : 1.2	-	LF(0.8, 1.25, 500, 180)
B	Ru3d3 Ru 0	A + 4.16	A * 1.917	A * 0.667	LF(1.01, 1.25, 500, 50)
C	Ru3d5 Ru 3	A + 1.25	0.5 : 1.5	-	LA(1, 1, 1121)
D	Ru3d3 Ru 3	C + 4.2	C * 1	C * 0.667	LA(1, 1, 1121)
E	Ru3d5 Ru 4	C + 1.4	C * 1	-	LA(1, 1, 1121)
F	Ru3d3 Ru 4	E + 4.14	C * 1	D * 0.667	LA(1, 1, 1121)
G	Ru3d5 Ru 5	C + 2.4	C * 1	-	LA(1, 1, 1121)
H	Ru3d3 Ru 5	G + 4.18	C * 1	G * 0.667	LA(1, 1, 1121)
I	C1s C-C	284.4 : 284.8	1.2 : 1.4	-	LA(1, 1, 1121)
L	C1s O-C=O	289 : 289.2	I * 1	-	LA(1, 1, 1121)

Table S17. Peak Fitting Model (NAP-XPS, CasaXPS) for the O 1*s* core level, with a Shirley background applied.

Ref.	Peak Label	Position (eV)	FWHM (eV)	Area Ratio	Line Shape
A	O1s M-O	-	0.9 : 1.4	-	LA(1, 1, 1121)
B	O1s O-H	A + 1.4	A * 1	-	LA(1, 1, 1121)
C	O1s O-C=O	A + 2.55	A * 1	-	LA(1, 1, 1121)

Table S18. Peak Fitting Model (NAP-XPS, CasaXPS) for the overlapping Y 3*d* and Zr 3*d* core levels, with a Shirley background applied.

Ref.	Peak Label	Position (eV)	FWHM (eV)	Area Ratio	Line Shape
A	Y3d5 Y-O	-	0.9 : 1.4	-	LA(1, 1, 1121)
B	Y3d3 Y-O	A + 2.06	A * 1	A * 0.667	LA(1, 1, 1121)
C	Y3d5 YCO3	A + 0.92	A * 1	-	LA(1, 1, 1121)
D	Y3d3 YCO3	C + 1.95	A * 1	C * 0.667	LA(1, 1, 1121)
E	Zr3d5 Zr-O	-	0.5 : 1.3	-	LA(1, 1, 1121)
F	Zr3d3 Zr-O	E + 2.39	E * 1	E * 0.667	LA(1, 1, 1121)

Data processing

NAP-XPS data was processed by (1) setting the base line to zero, and (2) calibrating the binding energy to that of the Zr $3d_{5/2}$ signal of lattice Zr^{4+}, which is set to 181.4 eV (the position observed in *ex situ* measurements). This was followed by intensity normalisation. The Ru 3*d* core level was normalised to the intensity of the neighbouring Y $3p_{3/2}$ peak, while the Zr 3*d*, Y 3*d* and O 1*s* core levels were all normalised to the intensity of the Y $3d_{5/2}$ signal. The Y $3d_{5/2}$ and $3p_{3/2}$ signals were chosen for intensity normalisation because they are expected to remain fairly stable over the range of measurement conditions. The Zr $3d_{5/2}$ signal assigned to lattice Zr^{4+} was chosen for binding energy calibration to address the unreliability of the C 1*s* C-C peak under the highly reducing measurement environment; as the Fermi level is shifted upwards by vacancies introduced under reducing conditions, the assumption of a common Fermi level between adventitious carbon and sample is no longer reliable.

Transmission electron microscopy

Particle size analysis

An estimate for the average size of exsolved Ru nanoparticles was obtained by collecting a series of TEM images of consistent magnification (300,000x), using ImageJ to demarcate and calculate the area of exsolved particles, then extracting an equivalent circular diameter from the calculated particle areas. Owing to the difficulty in accurately identifying exsolved particles with diameters of less than 1 nm, a cut-off of 1 nm was set for the threshold beyond which identified particles could contribute towards particle size analysis. Any particles with diameters below this threshold were discounted. Histograms of the observed particle size distributions are plotted in Figure S10, with the corresponding mean diameters provided in Table S19. Reliable estimates for the mean diameter could only be obtained for the samples reduced at 800 and 1000 °C; those reduced at 400 and 600 °C did not have a sufficient number of particles above the cut-off for a reliable estimate to be obtained.

Table S19. Particle size analysis performed on TEM images obtained from $Y_2Zr_{1.8}Ru_{0.2}O_7$ reduced at temperatures in the range 400 – 1000 °C.

R_T (°C)	Images analysed	Particle count	Particle count (d > 1 nm)	Mean diameter (nm)	Standard deviation (nm)
400	11	36	0	-	-
600	10	47	10	-	-
800	18	224	120	1.3	0.7
1000	14	206	193	1.9	0.7

Surface area and porosity analysis

Specific surface area and pore size characterisation

Table S20. Results of specific surface area and average pore size analysis for $Y_2Zr_{1.8}Ru_{0.2}O_7$ before and after reduction at 1000 °C.

Sample	Test No.	BET surface area (m^2/g)	σ (m^2/g)	C	R^2	Average pore width (BJH desorption) (nm)	Average pore width (desorption) (nm)
$Y_2Zr_{1.8}Ru_{0.2}O_7$	1	8.11	0.06	272	0.9998	19.6	12.0
	2	7.48	0.07	678	0.9997	20.0	12.3
$Y_2Zr_{1.8}Ru_{0.2}O_7$-R10	1	7.72	0.06	124	0.9998	18.3	11.3
	2	7.16	0.06	244	0.9998	17.2	11.7

Figures

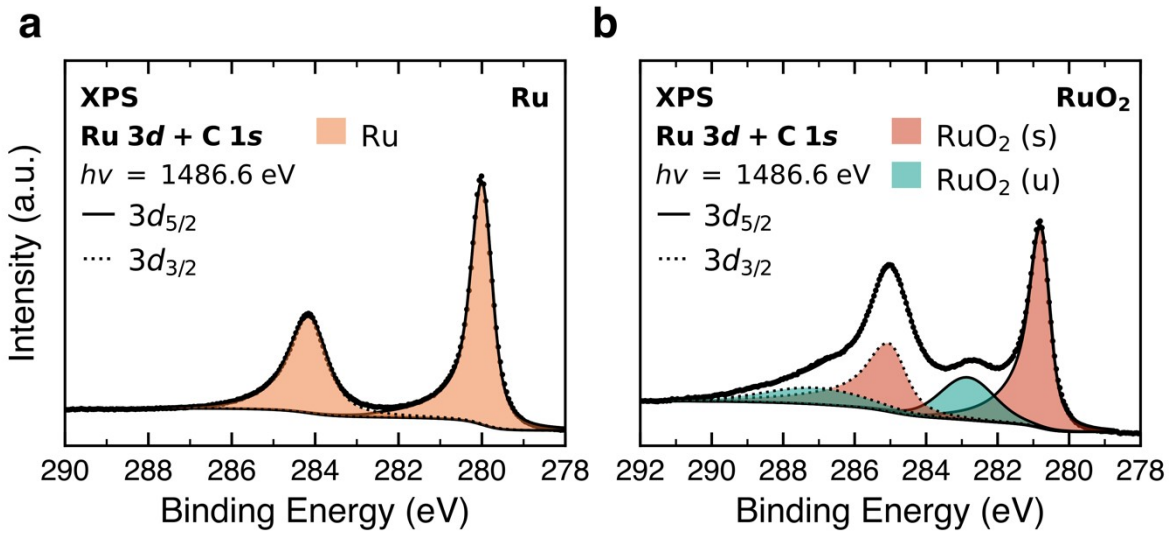

Figure S1. Fitted Ru 3*d* core level spectra of reference samples of (a) Ru and (b) RuO_2.

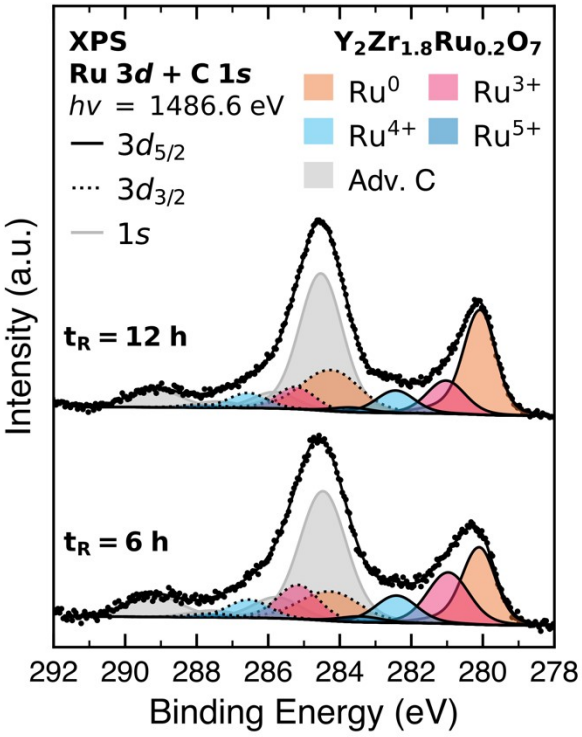

Figure S2. Ru 3*d* core level region of the photoelectron spectra of $Y_2Zr_{1.9}Ru_{0.1}O_7$ reduced with isothermal holds of (a) 6 hours and (b) 12 hours, at 800 °C under flowing 5% H2/N2, with a 5 °C /min ramp rate.

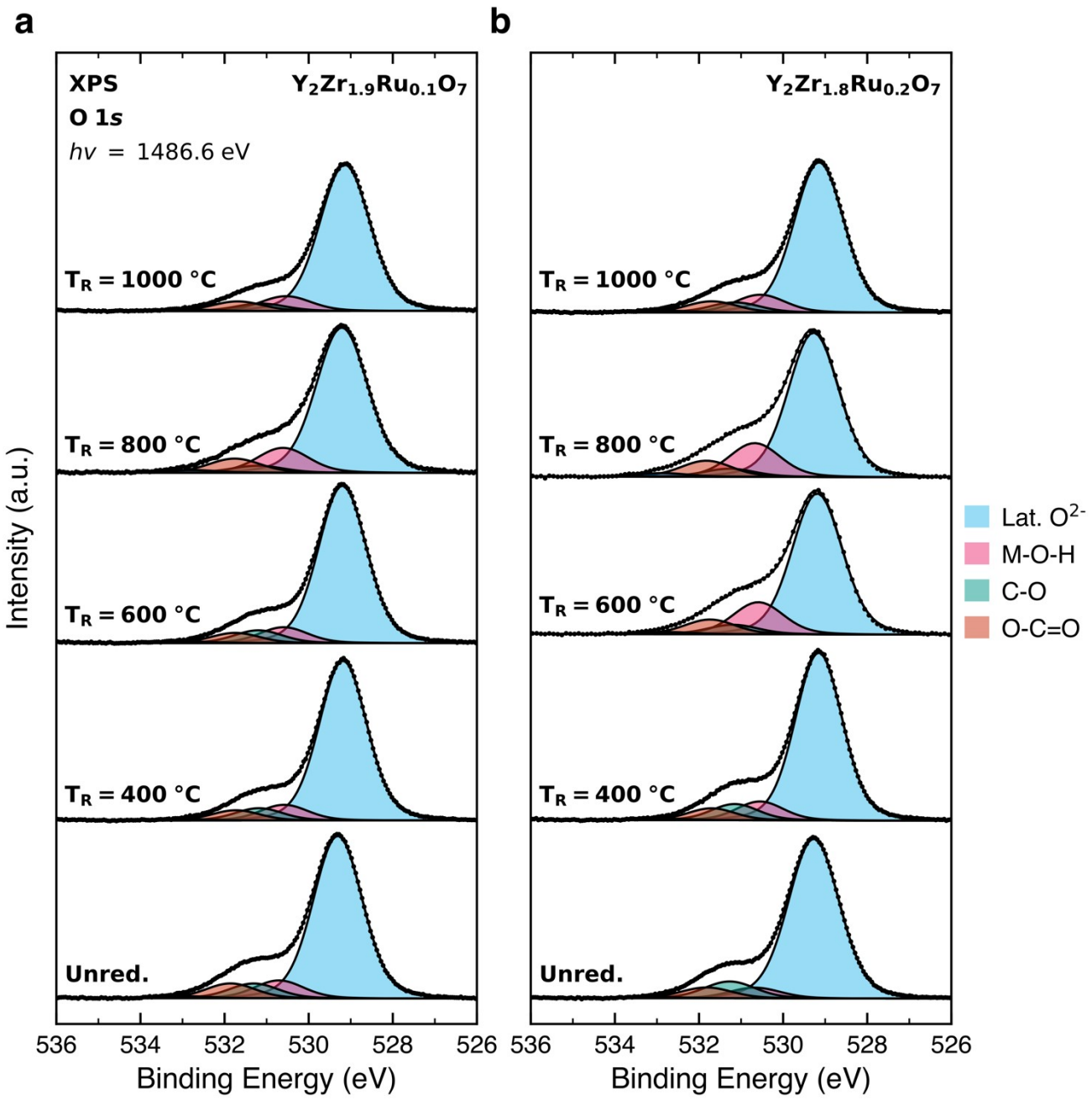

Figure S3. O 1*s* core level region of the photoelectron spectra of $Y_2Zr_{1.9}Ru_{0.1}O_7$ (a) $Y_2Zr_{1.8}Ru_{0.2}O_7$ (b) as a function of reduction temperature (T_R = 400, 600, 800, 1000 °C), with measurements before reduction included as a reference. All reduction procedures consisted of a 6h isothermal hold at the specified temperature under flowing 5% H_2/N_2, with a 5 °C/min ramp rate.

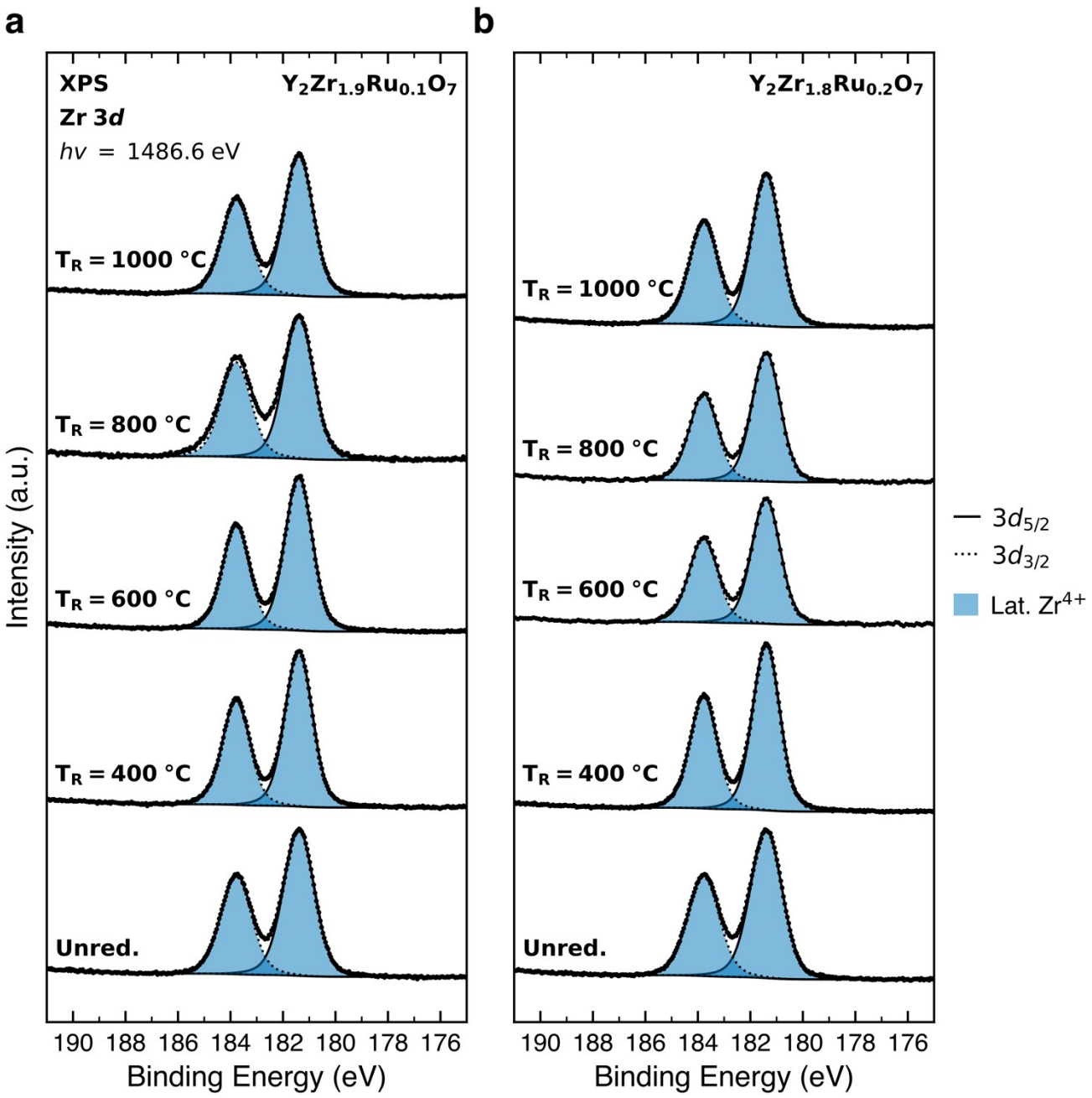

Figure S4. Zr 3*d* core level region of the photoelectron spectra of $Y_2Zr_{1.9}Ru_{0.1}O_7$ (a) $Y_2Zr_{1.8}Ru_{0.2}O_7$ (b) as a function of reduction temperature (T_R = 400, 600, 800, 1000 °C), with measurements before reduction included as a reference. All reduction procedures consisted of a 6h isothermal hold at the specified temperature under flowing 5% H_2/N_2, with a 5 °C/min ramp rate.

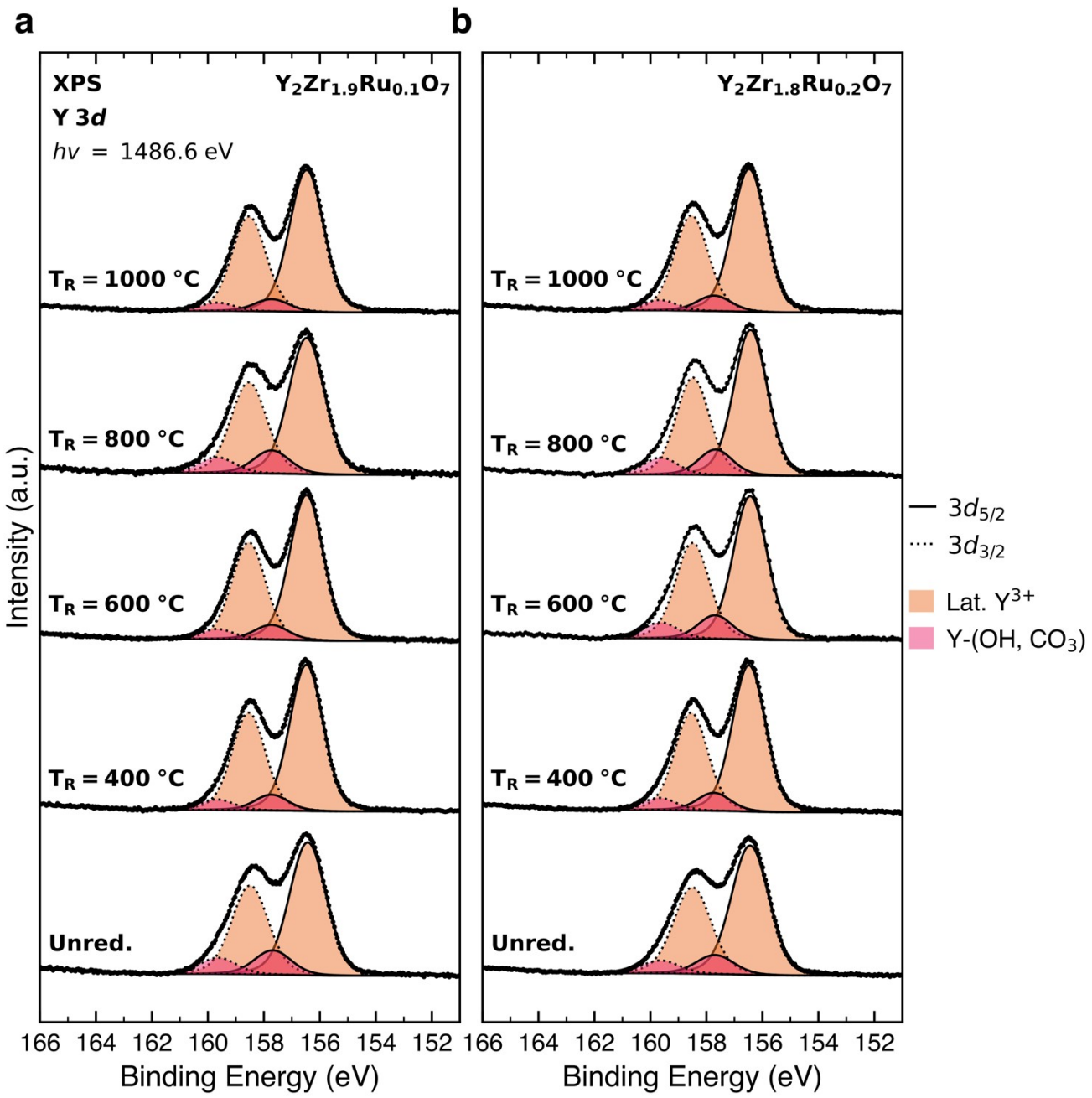

Figure S5. Y 3*d* core level region of the photoelectron spectra of $Y_2Zr_{1.9}Ru_{0.1}O_7$ (a) $Y_2Zr_{1.8}Ru_{0.2}O_7$ (b) as a function of reduction temperature (T_R = 400, 600, 800, 1000 °C), with measurements before reduction included as a reference. All reduction procedures consisted of a 6h isothermal hold at the specified temperature under flowing 5% H_2/N_2, with a 5 °C/min ramp rate.

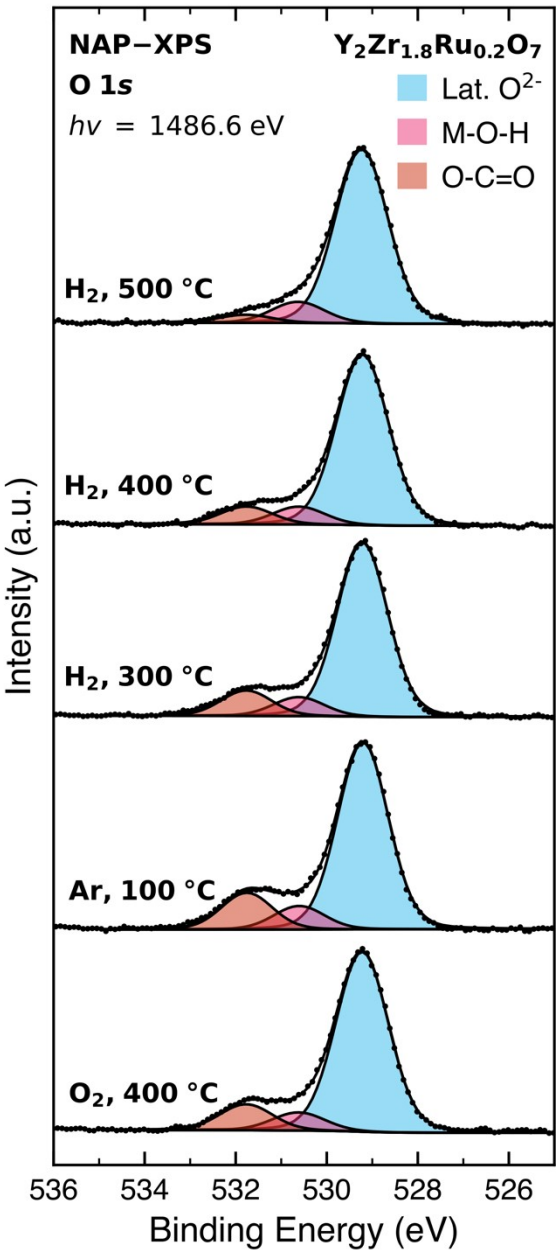

Figure S6. *In situ* NAP-XPS measurements of the O 1*s* core level region of the photoelectron spectrum of $Y_2Zr_{1.8}Ru_{0.2}O_7$. Spectra were acquired sequentially under the following series of conditions and averaged over their respective acquisition times (t_a): (1) 0.5 mbar O_2, 400 °C, t_a = 100 h (2) 0.5 mbar Ar, 100 °C, t_a = 80 h (3) 0.5 mbar H_2, 300 °C, t_a = 60 h (4) 0.5 mbar H_2, 400 °C, t_a = 60 h (5) 0.5 mbar H_2, 500 °C, t_a = 60 h.

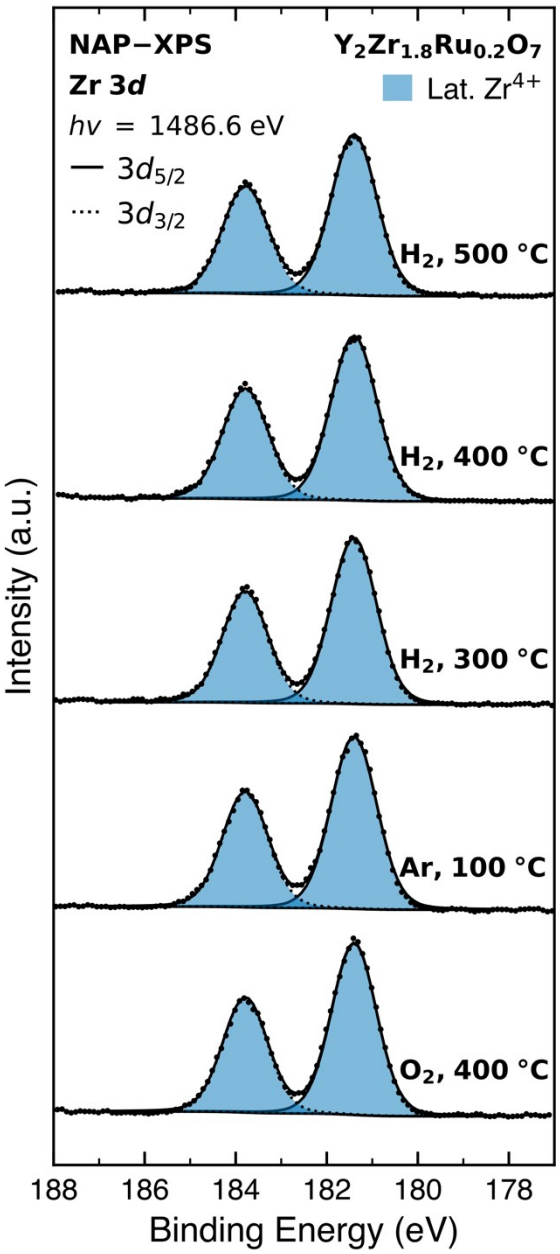

Figure S7. *In situ* NAP-XPS measurements of the Zr 3*d* core level region of the photoelectron spectrum of $Y_2Zr_{1.8}Ru_{0.2}O_7$. Spectra were acquired sequentially under the following series of conditions and averaged over their respective acquisition times (t_a): (1) 0.5 mbar O_2, 400 °C, t_a = 100 h (2) 0.5 mbar Ar, 100 °C, t_a = 80 h (3) 0.5 mbar H_2, 300 °C, t_a = 60 h (4) 0.5 mbar H_2, 400 °C, t_a = 60 h (5) 0.5 mbar H_2, 500 °C, t_a = 60 h.

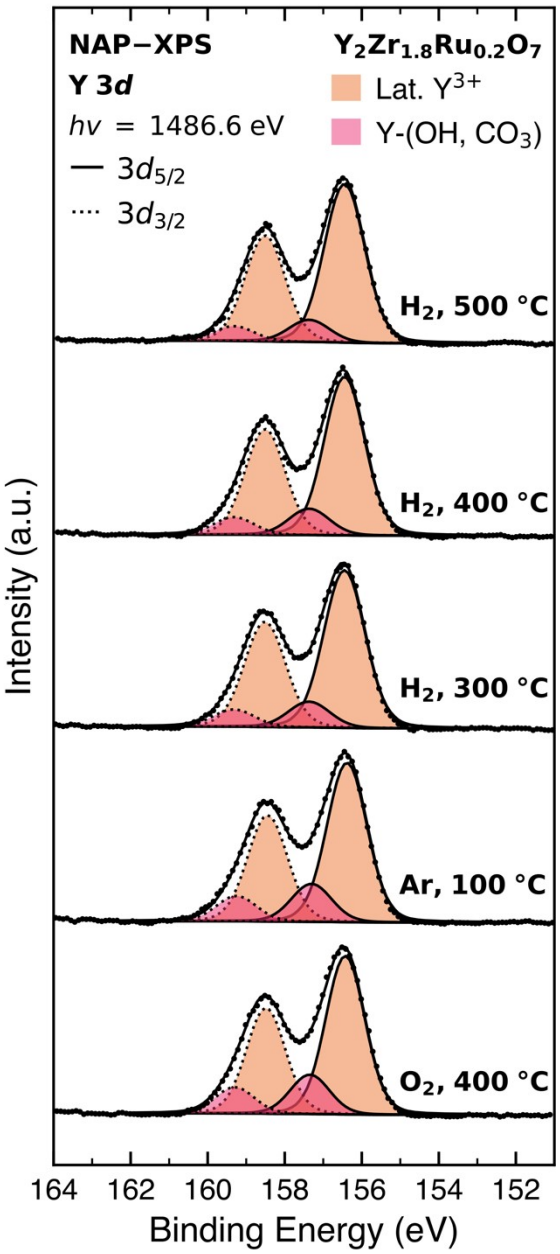

Figure S8. *In situ* NAP-XPS measurements of the Y 3*d* core level region of the photoelectron spectrum of $Y_2Zr_{1.8}Ru_{0.2}O_7$. Spectra were acquired sequentially under the following series of conditions and averaged over their respective acquisition times (t_a): (1) 0.5 mbar O_2, 400 °C, t_a = 100 h (2) 0.5 mbar Ar, 100 °C, t_a = 80 h (3) 0.5 mbar H_2, 300 °C, t_a = 60 h (4) 0.5 mbar H_2, 400 °C, t_a = 60 h (5) 0.5 mbar H_2, 500 °C, t_a = 60 h.

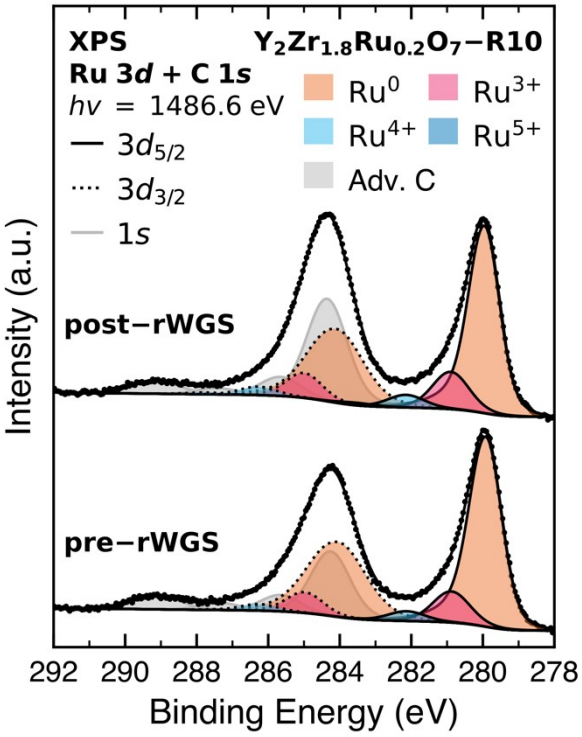

Figure S9. Ru 3d core level region of the photoelectron spectra of $Y_2Zr_{1.8}Ru_{0.2}O_7$ -R10 before and after testing for the reverse-water-gas-shift reaction.

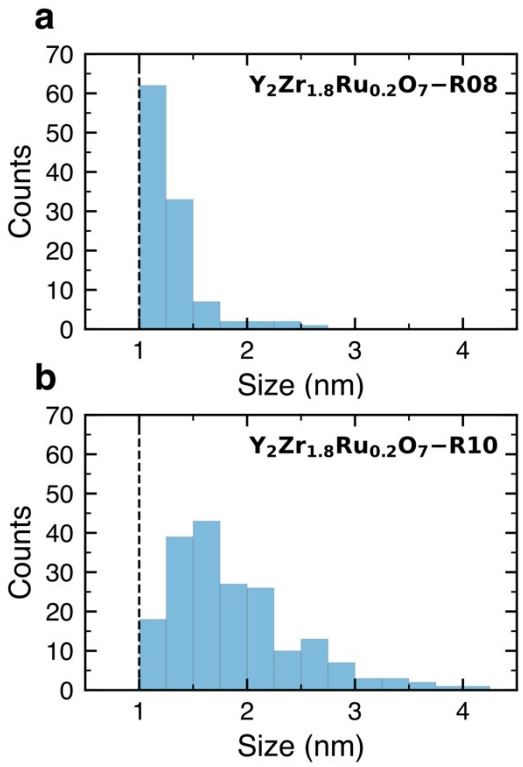

Figure S10. Comparison of the particle size distributions obtained from TEM analysis of $Y_2Zr_{1.8}Ru_{0.2}O_7$ reduced at 800 °C (a) and 1000 °C (b). Reduction procedures consisted of a 6h isothermal hold at the specified temperature under flowing 5% H_2/N_2, with a 5 °C/min ramp rate.

References

1 C. C. Fulton, T. E. Cook, Jr., G. Lucovsky and R. J. Nemanich, *Journal of Applied Physics,* 2004, **96**, 2665–2673.

2 P. Lackner, Z. Zou, S.Mayr, Ulrike Diebold and Michael Schmid, *Physical Chemistry Chemical Physics*, 2019, **21**, 17613-17620

3 D. J. Morgan, *Surface and Interface Analysis*, 2015, **47**(11), 1072-1079.